Identification of new turbulence contributions to plasma transport and confinement in spherical tokamak regime

W. X. Wang,* S. Ethier, Y. Ren, S. Kaye, J. Chen, and E. Startsev

Plasma Physics Laboratory, Princeton University,

P.O. Box 451, Princeton, NJ 08543, USA

Z. Lu

University of California, San Diego, La Jolla, CA 92093, USA

Z. Q. Li

Zhejiang University, P. R. China

Abstract

Highly distinct features of spherical tokamaks (ST), such as NSTX and NSTX-U, result in a different fusion plasma regime with unique physics properties compared to conventional tokamaks. Nonlinear global gyrokinetic simulations critical for addressing turbulence and transport physics in the ST regime have led to new insights. The drift wave Kelvin-Helmholtz (KH) instability characterized by intrinsic mode asymmetry is identified in strongly rotating NSTX L-mode plasmas. While the strong $\mathbf{E} \times \mathbf{B}$ shear associated with the rotation leads to a reduction in KH/ITG turbulence, the remaining fluctuations can produce a significant ion thermal transport that is comparable to the experimental level in the outer core region (with no "transport shortfall"). The other new, important turbulence source identified in NSTX is the dissipative trapped electron mode (DTEM), which is believed to play little role in conventional tokamak regime. Due to the high fraction of trapped electrons, long wavelength DTEMs peaking around $k_\theta \rho_s \sim 0.1$ are destabilized in NSTX collisionality regime by electron density and temperature gradients achieved there. Surprisingly, the $\mathbf{E} \times \mathbf{B}$ shear stabilization effect on DTEM is remarkably weak, which makes it a major turbulence source in the ST regime dominant over collisionless TEM (CTEM). The latter, on the other hand, is subject to strong collisional and $\mathbf{E} \times \mathbf{B}$ shear suppression in NSTX. DTEM is shown to produce significant particle, energy and toroidal momentum transport, in agreement with experimental levels in NSTX H-modes. Moreover, DTEM-driven transport in NSTX parametric regime is found to increase with electron collision frequency, providing one possible source for the scaling of confinement time observed in NSTX H-modes. Most interestingly, the existence of a turbulence-free regime in the collision-induced CTEM to DTEM transition, corresponding to a minimum plasma transport in advanced ST collisionality regime, is predicted.

PACS numbers: 52.35Ra, 52.25Fa, 52.25Fi, 52.65Tt

*Electronic address: wwang@pppl.gov

I. INTRODUCTION

The low-aspect ratio spherical tokamak (ST) experiments explore an alternative roadmap towards fusion energy production compared to that of conventional tokamaks. STs, such as the National Spherical Torus eXperiment (NSTX) and its upgrade NSTX-U, are characterized by high-β (the ratio of plasma pressure to magnetic pressure), very strong toroidal rotation due to neutral beam injected momentum, large ρ^* (the ratio of ion gyroradius to the plasma minor radius), strong toroidicity and shaping, etc. Such highly distinct features result in a different fusion plasma regime with unique physics properties, including transport and confinement behaviors, compared to conventional tokamaks.

In general, the free energy associated with non-uniform profiles of magnetically confined non-equilibrium plasmas drives various micro-instabilities in fusion experiments. The resulting turbulent fluctuations in electric and magnetic fields, density, temperature, and flows are responsible for anomalous particle, momentum and energy transport in such systems. In conventional tokamak regimes, drift wave instabilities of ion temperature gradient (ITG) mode and collisionless trapped electron mode (CTEM) are believed to be the prime sources for generating low-k fluctuations (about and larger than the ion gyroradius scale) and anomalous transport that are widely observed in experiments. In NSTX, high-k fluctuations of electron gyroradius scale are also observed, and could be one mechanism for driving anomalous electron transport. Low-k fluctuations, on the other hand, remain important in determining NSTX transport and confinement. This is supported by experimental observations that ion toroidal momentum transport is always much higher than neoclassical level and that ion energy transport is significantly anomalous in L-modes.[1] It is certainly possible that low-k fluctuations can also drive large energy transport in the electron channel, contributing to the highly anomalous level observed in experiments. However, the sources of low-k fluctuations in STs remain unclear. In particular, ST plasmas usually have a very large toroidal rotation that creates a strong $\mathbf{E}\times\mathbf{B}$ flow, and associated $\mathbf{E}\times\mathbf{B}$ flow shear are often strong enough to stabilize most of the low-k instability, including ITG and CTEM. We show that electron collisions can produce even stronger stabilizing effect on CTEM in the NSTX parametric regime. Important effects of STs on micro-instabilities also include: large trapped particle fraction; finite ρ^* (up to a factor of ten times greater in NSTX and NSTX-U than those of conventional tokamaks), which makes global effects particularly important for

transport; enhanced toroidicity and strong shaping, which impact the threshold and growth rate of microinstabilities,[2] trapped particle fraction, and zonal flow damping;[3] high-β, which may make electromagnetic effects much more important in determining plasma transport. Also because of these, it is crucial, while highly challenging, to use global gyrokinetic simulations to address instabilities, turbulence and transport physics in STs, taking into account the comprehensive influence of realistic geometry, collisionality, strong toroidal flow and associated $\mathbf{E} \times \mathbf{B}$ flow.

This nonlinear gyrokinetic study focuses on the investigation of distinct turbulence sources responsible for transport and confinement in the unique spherical tokamak regime. Two nontraditional turbulence sources found to be important in the ST regime through global gyrokinetic simulations of NSTX experiments are the drift wave Kelvin-Helmholtz (KH) instability and the dissipative trapped electron mode (DTEM). The topics to be discussed in this paper include: how KH mode and DTEM are identified; what are their linear and nonlinear features; what roles they play in driving plasma transport for NSTX and NSTX-U, namely, whether they drive experimentally relevant transport, and how they possibly contribute to the confinement scaling observed in STs. An interesting prediction is the potential existence of a minimum plasma transport state in advanced ST collisionality regime. Future experimental identification of KH and DTEM are also discussed.

The paper is organized as follows. Sec. II briefly describes the gyrokinetic simulation model used in this study. Sec. III presents linear and nonlinear studies of toroidal flow shear effects with a focus on the identification of the drift wave KH mode and the clarification of its contribution to NSTX transport. Identification of DTEM and its contribution to NSTX transport are presented in Sec. IV. DTEM is shown to survive the strong $\mathbf{E} \times \mathbf{B}$ shear, making it an important turbulence source that can dominate over CTEM under ST conditions. Collisionality dependence of both DTEM and CTEM-driven transport is discussed in Sec. V. In particular, DTEM-driven transport in the NSTX parametric regime is shown to produce the same trend as that of the confinement scaling observed in ST experiments. The existence of a minimum plasma transport regime that future advanced STs may access is predicted. In Sec. VI, the effect of short scale fluctuations on the ST confinement scaling is discussed. A summary and discussion are given in Sec. VII.

II. GYROKINETIC SIMULATION MODEL

In this work, our global turbulence simulation studies are carried out using the Gyrokinetic Tokamak Simulation (GTS) code.[4, 5] The GTS code is based on a generalized gyrokinetic simulation model using a δf particle-in-cell approach, and incorporates the comprehensive influence of non-circular cross section, realistic plasma profiles, plasma rotation, neoclassical physics, and Coulomb collisions.

First, we give a brief description of some of the latest features of GTS gyrokinetic simulation model applied to the studies reported in this paper. In the electrostatic limit (for this work), GTS solves the modern gyrokinetic equation in conservative form for the particle gyro-center distribution function $f_a(Z,t)$ of species-a as follows:[6]

$$\frac{\partial f_a}{\partial t} + \frac{1}{B^*}\nabla_{\mathbf{Z}} \cdot (\dot{\mathbf{Z}} B^* f_a) = \sum_b C[f_a, f_b]. \tag{1}$$

Here, $\mathbf{Z}$ represents the 5-dimensional gyro-center phase space variables, the equation of $\dot{\mathbf{Z}}$ describes the drift orbit of the gyro-center in phase space, $B^* = B + (m_a v_\parallel / e_a)\hat{\mathbf{b}} \cdot \nabla \times \hat{\mathbf{b}}$ with $\mathbf{b} = \mathbf{B}/B$, $v_\parallel$, e_a and m_a the parallel velocity, particle charge and mass respectively, and $C[f_a, f_b]$ is the Coulomb collision operator. Note that $\nabla_{\mathbf{Z}} \cdot (\dot{\mathbf{Z}} B^*) = 0$ represents the phase space incompressibility. Equation (1) is solved using a δf approach based on the principle of importance sampling, for which $f_a = (1 - \alpha \frac{e_a \delta\phi}{T_a}) f_{a,0} + \delta f_a$, where $f_{a,0}$ is a prescribed background distribution function, T_a is the background temperature, and $\delta\phi \equiv \phi - <\phi>$ is the total potential perturbation ϕ without its zonal potential $<\phi>$. The term -$\frac{e_a \delta\phi}{T_a} f_{a,0}$ represents the so-called adiabatic response, and α is a numerical factor set to $\alpha = 0$ for ions and $\alpha = 1$ or 0 for electrons. Eq. (1) can be rewritten as

$$\frac{\partial \delta f_a}{\partial t} + \frac{1}{B^*}\nabla_{\mathbf{Z}} \cdot (\dot{\mathbf{Z}} B^* \delta f_a) = -(1 - \alpha \frac{e_a \delta\phi}{T_a}) \frac{1}{B^*} \nabla_{\mathbf{Z}} \cdot (\dot{\mathbf{Z}} B^* f_{a0}) + \alpha [\frac{\partial}{\partial t}(\frac{e_a \delta\phi}{T_a}) + \frac{1}{B^*}\nabla_{\mathbf{Z}} \cdot (\dot{\mathbf{Z}} B^* \frac{e_a \delta\phi}{T_a}] + \sum_b (C^l + C_0), \tag{2}$$

where

$$C^l(\delta f_a) = C[\delta f_a, (1 - \alpha \frac{e_b \delta\phi}{T_b}) f_{b,0}] + C[\delta f_b, (1 - \alpha \frac{e_a \delta\phi}{T_a}) f_{a,0}]$$

is a linearized collision operator, and

$$C_0 = C[(1 - \alpha \frac{e_a \delta\phi}{T_a}) f_{a,0}, (1 - \alpha \frac{e_b \delta\phi}{T_b}) f_{b,0}].$$

Note that both turbulent and neoclassical physics are included in Eq.(2). Comparing to Eq.

(1), the only approximation used in Eq. (2) is the neglect of the nonlinear collision terms $C[\delta f_a, \delta f_b]$.

For clarity of presentation, we now focus our discussion on ions ($\alpha = 0$), without losing generality. Most naturally, the background f_0 is chosen to be the neoclassical equilibrium solution, which satisfies

$$\frac{1}{B^*}\nabla_Z \cdot (\dot{\mathbf{Z}}_0 B^* f_{a0}) = \sum_b C_0(f_0), \tag{3}$$

where $\dot{\mathbf{Z}}_0$ describes unperturbed drift orbits, including the magnetic drift and the equilibrium $\mathbf{E} \times \mathbf{B}$ drift. However, the neoclassical equilibrium solution is unknown analytically. Consequently, a shifted Maxwellian distribution with either model or experimental density, temperature and toroidal rotation profiles is taken to be the background f_0. Eq. (2) becomes

$$\frac{\partial \delta f}{\partial t} + \frac{1}{B^*}\nabla_{\mathbf{Z}} \cdot (\dot{\mathbf{Z}} B^* \delta f) = -\frac{1}{B^*}\nabla_{\mathbf{Z}} \cdot (\dot{\mathbf{Z}} B^* f_{SM}) + C^l(\delta f). \tag{4}$$

Here, we neglect the ion-electron collisions since they are much less frequent than the ion-ion collisions. Again, the neoclassical physics is retained in Eq. (4). By replacing $\dot{\mathbf{Z}}$ with $(\dot{\mathbf{Z}} - \dot{\mathbf{Z}}_0)$ in the first term of the right hand side of the equation above, the neoclassical physics is removed. This is equivalent to assuming that f_{SM} is the neoclassical equilibrium solution of Eq. (3). Consequently, it is optional in GTS to either i) include neoclassical physics in turbulence simulations self-consistently, or ii) take a neoclassical radial electric field as an input into the turbulence simulation.

In the δf particle-in-cell approach for solving the kinetic equations, a particle weight "w" is introduced as a new dimension in addition to the physical phase space $\mathbf{Z}$.[7] Specifically, for solving Eq. (4), the marker particle distribution function $F(\mathbf{Z}, w, t)$ in the extended phase space $(\mathbf{Z}, w)$ is advanced according to the following kinetic equation:

$$\frac{\partial F}{\partial t} + \frac{1}{B^*}\nabla_Z \cdot (\dot{\mathbf{Z}} B^* F) + \frac{\partial}{\partial w}(\dot{w} F) = C^l(F). \tag{5}$$

The equation of $\dot{\mathbf{Z}}$ describes the gyrocenter trajectories in the physical phase space $\mathbf{Z}$. The equation for the particle weight is

$$\dot{w} = \frac{1-w}{f_{SM}}\left[-\frac{1}{B^*}\nabla_Z \cdot (\dot{\mathcal{Z}} B^* f_{SM})\right] + \eta(w - \langle w \rangle), \tag{6}$$

where $\dot{\mathcal{Z}} = \dot{\mathbf{Z}}$ or $(\dot{\mathbf{Z}} - \dot{\mathbf{Z}}_0)$ corresponds to with or without self-consistent neoclassical physics, respectively, $\langle w \rangle = \int dw F w / \int dw F$ is an average weight, and η is a function independent

of w and to be determined later. The weight Eq. (6) is determined by requiring that the marker particle kinetic equation, Eq. (5), can reproduce Eq. (4) with $\delta f = \int dwFw$. This can be readily proven by following the procedure given in Ref. 8.

Now we determine the function η. It is very important to note that, in particle simulations, the distribution function is sampled by markers and is evolved by advancing these markers along phase space trajectories according to $d\mathbf{Z}/dt = \dot{\mathbf{Z}}$ and $dw/dt = \dot{w}$, and subjected to Coulomb collisions. This actually solves the following equation:

$$\frac{\partial F}{\partial t} + \dot{\mathbf{Z}} \cdot \nabla_Z F + \dot{w}\frac{\partial F}{\partial w} = C^l(F). \tag{7}$$

Therefore, equating Eq. (7) to Eq. (5) results in $\partial\dot{w}/\partial w = 0$, in addition to $\nabla_{\mathbf{Z}} \cdot (\dot{\mathbf{Z}}B^*) = 0$. Namely, the extended phase space $(\mathbf{Z}, w)$ is also incompressible. This determines the function η in Eq. (5) and results in an accurate weight equation given by

$$\dot{w} = \frac{1-w}{f_{SM}}(-\dot{\mathcal{Z}} \cdot \nabla_{\mathbf{Z}} f_{SM}) + \frac{w - \langle w \rangle}{f_{SM}}(-\dot{\mathcal{Z}} \cdot \nabla_{\mathbf{Z}} f_{SM}). \tag{8}$$

When compared to other weight schemes that are widely used in many δf codes, our scheme contains an extra term on the right hand side (second term), which is essential to ensure phase space incompressibility $\partial\dot{w}/\partial w = 0$.

The electrical potential ϕ is obtained from solving a gyrokinetic Poisson equation as follows:[9]

$$-\nabla_\perp \cdot \frac{Z_i n_{i,0}}{B\Omega_i}\nabla_\perp \phi = \delta\bar{n}_i - \delta n_e, \tag{9}$$

where Ω_i and Z_i are the ion cyclotron frequency and charge number, respectively, $n_{i,0}$ is the equilibrium ion density, and $\delta\bar{n}_i$ and δn_e are the total ion and electron density fluctuations, respectively. GTS used to solve the gyrokinetic Poisson equation in integral form[10]. Now, Eq. (9) is solved by using a finite element based solver on a triangular mesh in general tokamak geometry and flux coordinates. More specifically, we can separate Eq. (9) into two coupled equations for the turbulent potential $\delta\phi$ and the zonal potential $< \phi >$, respectively, and solve them iteratively.

III. FLOW SHEAR DRIVEN DRIFT WAVE KELVIN-HELMHOLTZ INSTABILITY

It is generally believed that the prospects for achieving high quality plasma performance in magnetically-confined plasmas will be significantly enhanced by optimizing plasma flow

characteristics. This can play a critical role in both controlling macroscopic plasma instabilities (e.g., resistive wall mode, neoclassical tearing mode, etc) and in reducing energy loss due to plasma micro-turbulence.

A. Impact of toroidal flow on low-k instabilities via its contribution to E×B shear effect

In toroidal fusion devices, plasmas can rotate in both toroidal and poloidal directions. The toroidal rotation V_ϕ usually dominates over the poloidal rotation V_θ, which is subject to strong damping due to the magnetic pumping effect. The toroidal rotation can strongly impact micro-instabilities, particularly long wavelength modes, through its contribution to the equilibrium electric field

$$E_r = \frac{1}{c}(B_\theta V_\phi - B_\phi V_\theta) + \frac{1}{ne}\frac{\partial p}{\partial r},$$

for which the associated $\mathbf{E} \times \mathbf{B}$ flow shear can change instability growth rate linearly and cause turbulence decorrelation nonlinearly.[11] Here, B_ϕ and B_θ are the toroidal and poloidal magnetic field components, respectively, and p is the ion pressure. In NSTX, toroidal rotation is largely driven by the momentum injection associated with neutral beam heating, and toroidal rotation contribution to E_r usually dominates over the poloidal rotation and the pressure gradient term.

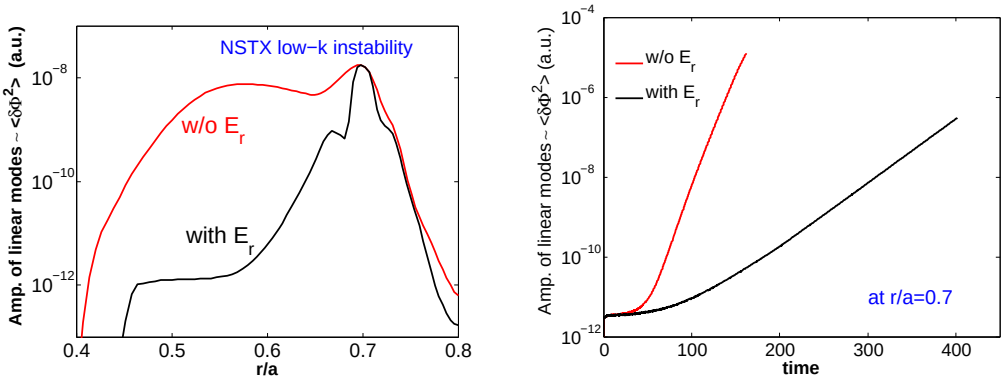

FIG. 1: Radial profiles of linear mode intensity $\sim< \delta\Phi^2 >$ (left), and the time histories of the mode intensity at the radial location of strongest instability (right) from simulations of an NSTX discharge with and without equilibrium E_r.

A typical example of equilibrium $\mathbf{E} \times \mathbf{B}$ shear effects on low-k instabilities in NSTX are shown in Fig. 1. The results are obtained from linear, multi-mode, global simulations of an NBI-heated L-mode discharge. It is shown that the strong $\mathbf{E} \times \mathbf{B}$ shear flow, mainly contributed by NBI-driven toroidal rotation, suppresses low-k instabilities over a wide radii (left panel of Fig. 1). At the radial location of strongest instability, the average growth rate is reduced by factor of five (right panel of Fig. 1). In practice, particularly for analyzing experimental data, a widely used stability criteria for looking at $\mathbf{E} \times \mathbf{B}$ shear effects[12] is to compare the $\mathbf{E} \times \mathbf{B}$ shearing rate[13] to the instability growth rate. While this rule is useful, the real physics goes well beyond the over-simplified picture, involving the effects on mode structure. Generally, the $\mathbf{E} \times \mathbf{B}$ shear effects on instabilities is strongly mode-dependent, varying case by case. As in Fig. 2, which illustrates the most unstable trapped electron modes for an NSTX H-mode case, the $\mathbf{E} \times \mathbf{B}$ shear is shown to change the unstable mode family member and structure. The mostly unstable modes have toroidal mode number $n > 25$ in the absence of equilibrium $\mathbf{E} \times \mathbf{B}$ flow, in comparison to $n < 25$ in the presence of the $\mathbf{E} \times \mathbf{B}$ flow. Moreover, it is also shown that the $\mathbf{E} \times \mathbf{B}$ shear flow can shift modes off the rational surface specified by $m/n = q(r)$ (safety factor), which is indicated by the red lines in Fig. 2. This results in a finite parallel wavenumber $k_{\|} \sim \hat{b} \cdot \nabla\theta(m - nq)$, which enhances Landau damping for the modes, causing a reduction in the growth rate. This is also one mechanism that $\mathbf{E} \times \mathbf{B}$ shear may make modes less unstable.

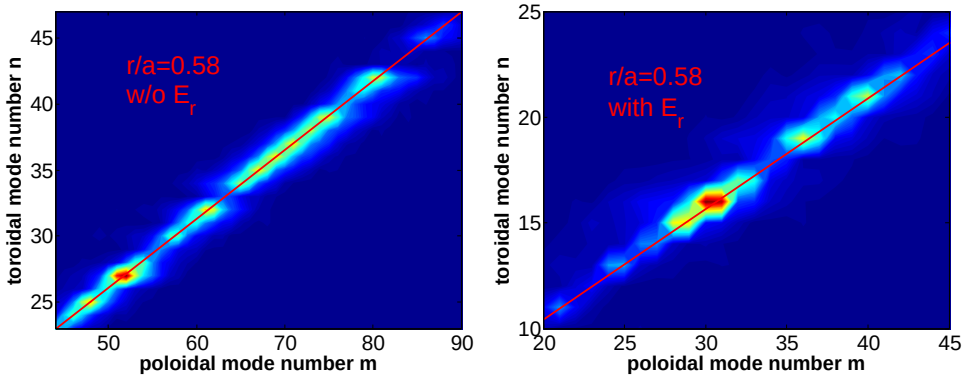

FIG. 2: Linear TEM mode spectrum, $\delta\Phi^2_{m,n}$, from simulations with (right) and without (left) equilibrium E_r for an NSTX H-mode case, indicating the locations of the most unstable modes in (m, n) space. The red lines indicate the mode rational surface with $m/n = q(r)$.

B. Generic features of flow shear driven Kelvin-Helmholtz mode in toroidal plasmas

The velocity shear also provides a source of free energy which may drive its own instability and turbulence in magnetized plasmas.[14] This is known as the drift-wave-type Kelvin-Helmholtz (KH) instability.[15–19] For parallel velocity shear, the instability occurs due to ion parallel bunching caused by cross-field convection of parallel flow. The associated electric field reinforces the convection, providing a positive feedback. It is worth pointing out that the velocity shear driven mode in plasmas is basically a drift wave like other pressure gradient driven modes, such as ITG, and is fundamentally different from the well-studied Kelvin-Helmholtz fluid instability due to velocity shear in a single continuous fluid, or velocity difference across the interface between two fluids.

In the past, the drift KH instability attracted a lot of interest in plasma physics research. The theoretical studies carried out at the time were mostly linear analyses in sheared slab magnetic geometry and were based on the fluid model. More recent nonlinear gyrokinetic simulations of ion temperature gradient turbulence in toroidal plasmas observed enhanced transport in the high parallel velocity shear regime following the usual transport reduction due to the equilibrium $\mathbf{E} \times \mathbf{B}$ shear effect at medium flow shear regime,[20–22] suggesting that a strong flow shear may trigger a new instability responsible for the observed transport enhancement. However, direct gyrokinetic studies of drift-KH mode, in particular nonlinear studies, are still very limited.

In this section, we first examine the generic features of drift-KH in toroidal plasmas using global gyrokinetic simulations. The simulation study, which includes kinetic electrons, is carried out using a DIII-D-size conventional tokamak geometry. We choose the temperature and density gradients for electrons and ions to be small in order to make ITG and TEM, which are two major turbulence sources in conventional tokamaks, stable. Specifically, the ratios of major radius over gradient scale lengths are $R_0/L_{T_i} = R_0/L_{T_e} = R_0/L_n = 1.2$. A large toroidal rotation gradient is set up in the central core region, as shown in the left panel of Fig. 3. The mode growth rate and frequency are illustrated in the middle panel of Fig. 3, which shows that strong flow shear can drive low-k modes, roughly in the same range as ITG mode. The modes have roughly a constant growth rate, weakly depending on k_θ, unlike ITG which typically peaks near $k_\theta \rho_s = 0.5$.

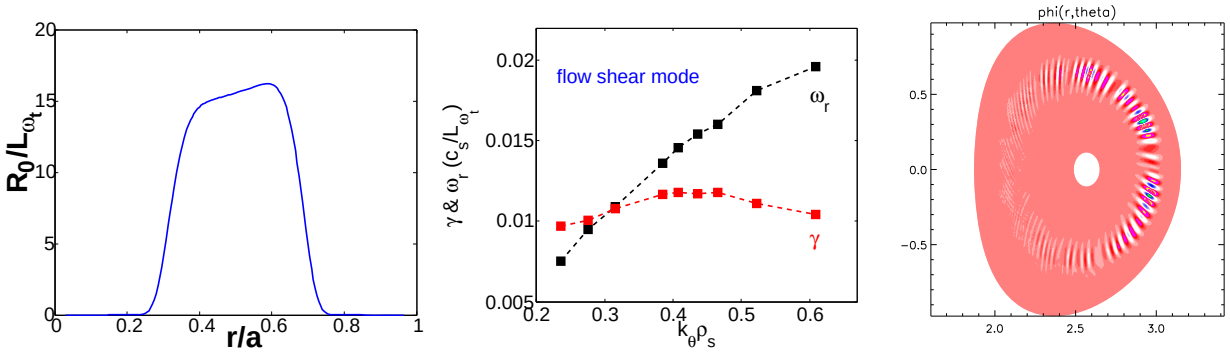

FIG. 3: Radial profiles of toroidal rotation gradient used for drift-KH simulations (left), linear growth rate γ and real frequency ω_r of KH modes vs poloidal wavenumber k_θ (middle), and contour plot of electric potential of KH modes (right).

One remarkable feature of drift-KH mode, which is distinct from most drift wave instabilities, is that the eigenfunction is intrinsically shifted off its rational surface. Figure 4 shows the locations of the most unstable modes in the m, n space for drift-KH (left), ITG (middle) and CTEM (right). The dotted lines in the plots indicate the mode rational surface $m/n = q(r)$. Unlike the ITG and CTEM modes, most of the KH modes are located away from their rational surface. Note that this is not caused by the mean $\mathbf{E}\times\mathbf{B}$ shear, which is not included in these simulations. In other words, there is an intrinsic asymmetry in the parallel wavenumber spectrum of KH modes, resulting in a finite $k_\| \sim \hat{b}\cdot\nabla\theta(m-nq)$. As a consequence, the KH modes are subjected to stronger Landau damping, reducing the growth rate and increasing the threshold of the instability. Moreover, the intrinsic $k_\|$-symmetry breaking in the KH mode structure may enhance Reynolds stress generation, which may strongly impact momentum transport [23] and poloidal flow generation, as proposed previously.[24, 25] However, it should be pointed out that it is the turbulence fluctuation spectrum structure, rather than its linear mode structure, that is critical in generating Reynolds stress. As we will see later, the significant intrinsic asymmetry present in the linear modes does not persist in the turbulence fluctuations due to nonlinear toroidal mode couplings. This suggests that the Reynolds stress generation may not be as significant as it seems in terms of the linear KH mode structure.

Now we discuss the nonlinear physics related to the saturation of the KH instability. Figure 5 shows how fluctuations evolve in k-space as the the KH instability develops towards

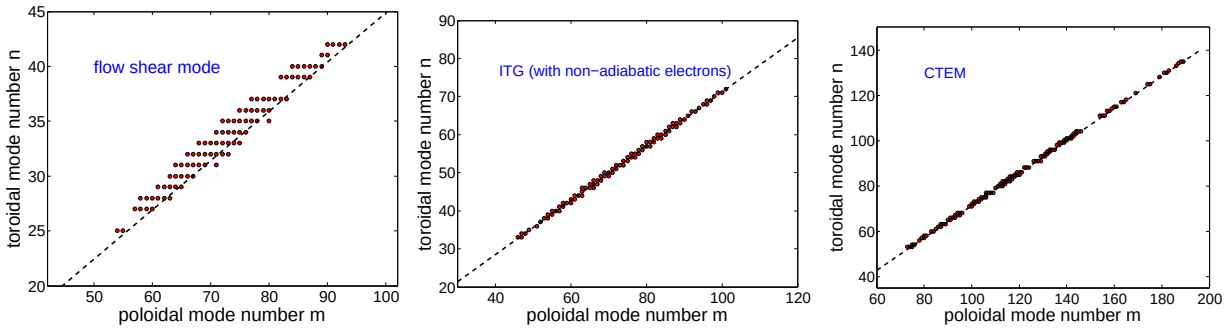

FIG. 4: Locations of the most unstable modes in poloidal and toroidal mode number (m, n) space for drift-KH (left), ITG (middle) and CTEM (right) instability. Dotted straight lines is $m/n = q(r)$, indicating the mode rational surface.

saturated turbulence state. At the early phase (top-left panel of Fig. 5), linearly unstable modes with toroidal mode number $n > 25$ are excited in the vicinity of the rational surface (with significant finite $k_\parallel$). At the stage when the instability gets saturated, longer wavelength modes with $n < 25$, which are linearly stable, are nonlinearly excited due to toroidal mode couplings (top-middle panel of Fig. 5). This process can be clearly identified through bi-coherence analysis. The resulting bi-spectrum is presented in the lower-left panel of Fig. 5, which shows a strong coupling of low-m modes (linearly stable) to linearly unstable modes. Note that the energy channeling for mode couplings in toroidal systems is highly selective. Namely, it occurs along a narrow band around the rational surface in k-space so as to minimize the parallel Landau damping. This is a characteristic feature of nonlinear toroidal mode coupling. The KH instability continuously pumps energy at the higher-k range in the nonlinear saturation state. A quasi-stationary turbulence state is reached by balancing the energy pumping (by KH instability) with energy redistribution in k-space (via nonlinear mode couplings) and dissipation. The steady state turbulence shows an overall down-shifted spectrum which is dominated by the nonlinearly excited modes at longer wavelength (see upper-right panel of Fig.5). The nonlinearly excited mode spectrum is shown to be localized along a narrow band centered around the rational surface and, as mentioned previously, the spectrum asymmetry that is present in the original linear KH modes has mostly disappeared. In this process, the nonlinear mode coupling due to the $\mathbf{E} \times \mathbf{B}$ nonlinearity seems to play a major role in the recovery of the spectrum symmetry in the longer wavelength fluctuations. The linear toroidal mode coupling which couples together different poloidal harmonics of

a single-n mode via the magnetic curvature term does not lead to the elimination of the spectrum asymmetry in the linear phase. The feature of the linear mode coupling appears unchanged in the nonlinear phase, and it does not have a major effect on the the spectrum symmetry recovery. In addition to the inverse energy cascading process described above, a strong generation of zonal flows is also observed (lower-right panel), which also plays a critical role in determining the turbulence saturation level.

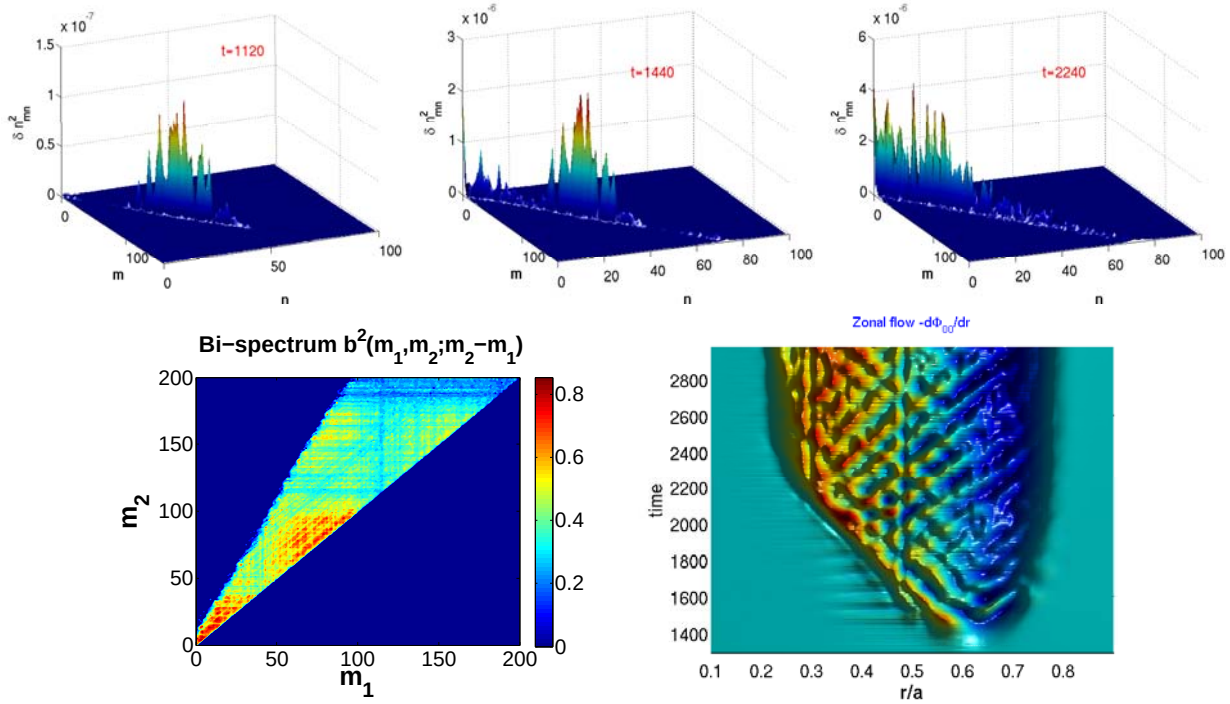

FIG. 5: Three time slices of the KH-driven density fluctuation spectra δn^2_{mn}: linear growth phase (upper-left), an earlier time during nonlinear saturation (upper-middle), and fully developed turbulence regime (upper-right); bi-spectrum $b^2(m_1, m_2; m_2 - m_1)$ showing the coupling of three mode m_1, m_2 and $(m_2 - m_1)$ (lower-left); and spatio-temporal evolution of zonal flow (lower-right). This nonlinear simulation uses the same parameters as in Fig. 3.

C. Kelvin-Helmholtz instability and associated turbulence transport in NSTX

The excitation of KH modes in toroidal plasmas requires a large toroidal rotation with a strong gradient to overcome various damping effects, including enhanced Landau damping due to finite $k_\parallel$, the magnetic shear stabilization, and the $\mathbf{E}\times\mathbf{B}$ shear suppression associated

with toroidal rotation gradient. This makes it harder to destabilize KH modes in toroidal plasmas compared to ITG and TEM. A rough evaluation of the threshold for KH excitation based on analytic calculations in simple geometry is [15, 19]

$$\left| \frac{ML_n}{L_{\omega_\phi}} \right| > 1, \tag{10}$$

where $M = V_\phi/c_s$ is the Mach number with the sound speed $c_s = \sqrt{T_e/m_i}$, $L\omega_\phi$ and L_n are the toroidal rotation and density gradient scale lengths, respectively. As indicated in Eq. 10, the density gradient is a stabilizing effect. As noticed previously, the threshold for destabilizing KH is hardly achievable for typical tokamak parameters.[11] Indeed, the KH modes have been observed in linear machines, but there is no report of observing KH in tokamak experiments, and neither a clear identification of the presence of KH modes from direct numerical simulations for realistic discharges.

However, the situation can be quite different in ST plasmas. Because of the smaller plasma volume, the external momentum injection provided by NBI can drive the ST plasma to rotate much faster than in conventional tokamaks, bringing it into a regime with $M \sim 1$ and a steep rotation gradient where the KH could be destabilized. The instability condition of Eq. 10 is examined for an NBI-heated L-mode NSTX discharge.[26] As shown in Fig. 6, fast rotation ($M \sim 1$) and steep rotation gradient make the KH drive well above the instability threshold in the central core region, suggesting the possible excitation of the mode. Direct linear and nonlinear global gyrokinetic simulations are then carried out for this experiment to provide a clear identification of the KH modes and their role in driving transport.

Unlike most drift wave instabilities in toroidal plasmas, the KH eigenmode structure displays an intrinsic asymmetry. This unique feature provides a clear way for its identification. Specifically, the KH modes shift off their rational surface as shown in Fig. 4, and correspondingly, have significant finite $k_\parallel$ proportional to the rotation gradient: [16, 19]

$$k_\parallel \sim \frac{k_\theta \rho_s}{2c_s} \frac{1}{n} \frac{d(nV_\parallel)}{dr} \sim \frac{d\omega_\phi}{dr}. \tag{11}$$

Our global simulations cover a radial domain from $r/a = 0.3$ to 0.8. The size of the grid cells on the poloidal planes is $\sim$ local ρ_i, and 200 particles/cell·species are used. The equilibrium $\mathbf{E} \times \mathbf{B}$ is set to be zero in our linear simulations. The simulated instability mode structures are illustrated in Fig. 7. Indeed, in the region where the condition of Eq. 10 is well satisfied,

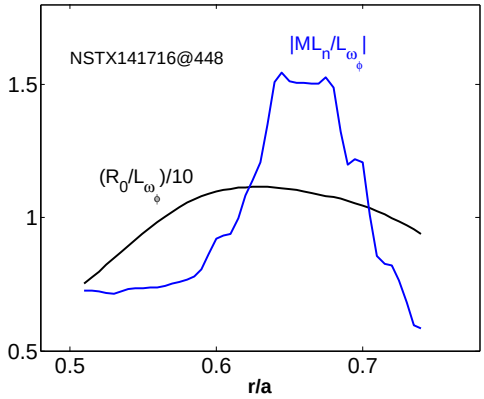

FIG. 6: Radial profile of $\left|ML_n/L_{\omega_\phi}\right|$ and toroidal rotation gradient for an NSTX L-mode shot.

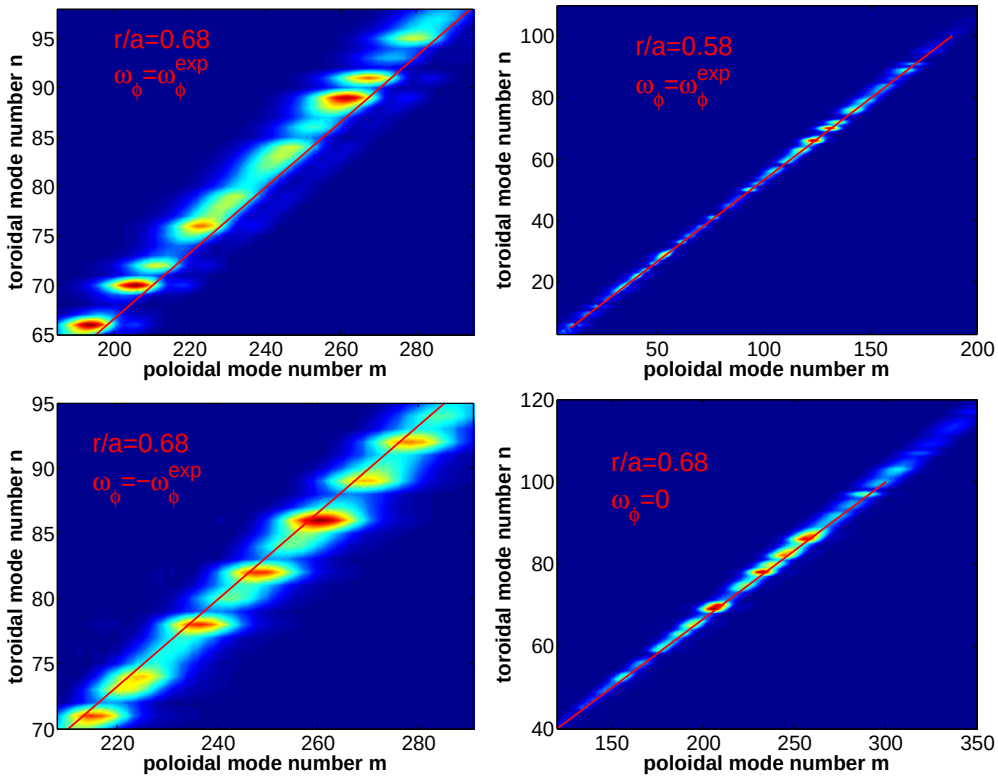

FIG. 7: Linear mode spectra $\delta\Phi_{mn}$ at two radial locations (flux surfaces) from simulations using different toroidal rotations: at $r/a = 0.68$ with real toroidal rotation (upper-left), $r/a = 0.58$ with real rotation (upper-right), $r/a = 0.68$ with inverse rotation (lower-left) and $r/a = 0.68$ with zero rotation (lower-right). Straight lines indicate mode rational surfaces.

the excited modes are located away from the rational surface to one side (upper-left panel of Fig. 7), showing a strong asymmetry. In contrast to this, in the region where the flow shear driver is weak (as indicated in Fig. 6), unstable modes are basically located on the rational surface (upper-right panel of Fig. 7), showing little asymmetry. Note that there is a significant ion temperature gradient in the region, which drives those ITG modes. Moreover, the direction to which the KH modes are shifted away from the rational surface depends on the sign of the rotation gradient. This can be seen from Eq. 11. This characteristic is further tested as a fingerprint of KH modes by a simulation in which we flip over the rotation profile, $\omega_\phi \to -\omega_\phi$. As shown in the lower-left panel of Fig. 7, the unstable modes in this case are shifted away to the other side of the rational surface, consistent with Eq. 11. Furthermore, we also carried out a simulation without toroidal rotation. In this case, only the ITG modes are excited, which are in a similar range of toroidal mode number as that of KH modes, but mostly located on the rational surface (lower-right panel of Fig. 7). Therefore, we conclude that the drift-wave KH modes are destabilized in NSTX plasmas by strong toroidal rotation with large gradient produced by NBI. For this specific discharge, both KH modes and ITGs co-exist, although the KH modes grow faster than ITGs.

Next, the nonlinear simulations of the same NSTX discharge are carried out to investigate the role of KH instability in driving plasma transport in NSTX. Our nonlinear simulations include both electron and ion collisions, and a self-consistent equilibrium radial electric field calculated from the radial force balance equation in terms of experimental pressure and toroidal rotation profiles, and a neoclassical poloidal flow. The strong toroidal rotation makes a dominant contribution to the equilibrium electric field for this NSTX case. The associated $\mathbf{E} \times \mathbf{B}$ shear is found to have strong influence on low-k fluctuations due to KH and ITG instabilities. Linearly, it largely reduces the growth rate of the mode and changes unstable mode family members and structure, as discussed in Sec. IIIA. Nonlinearly, it modifies fluctuation amplitude and spectrum. However, the equilibrium $\mathbf{E} \times \mathbf{B}$ shear does not fully suppress KH/ITG generated turbulence, and a finite fluctuations level remains. The upper-left panel of Fig. 8 shows a contour plot of potential fluctuations on a poloidal plane at the saturated turbulence state. The normalized potential fluctuation amplitude is about $e\delta\phi/T_e \sim 1\%$. The turbulence fluctuations consist of contributions from both KH and ITG modes. However, it is hard to distinguish one another because their wavenumbers are all in the low-k range, and because the intrinsic asymmetry in mode structure that

distinguishes the KH modes from the ITG modes disappears as the instability evolves into the turbulence state. It is noted that the KH turbulence might leave a footprint in the feature of transport asymmetry in the poloidal direction, namely, more prominent transport in the higher field side compared to ITG induced transport due to the difference in destabilizing mechanism. In fact, toroidal KH modes are also observed to balloon in the lower field side due to significant magnetic curvature effect in toroidal geometry (see the right of Fig. 3). The resulting turbulent fluctuations and transport appear more prominent in the lower field side, too, showing no significant difference than that of ITG. Since the KH growth rate is larger than ITG, the KH contribution to the fluctuation may dominate over ITG in this NSTX case. As shown in the time history of various diffusivities (upper-right of Fig. 8), the remaining low-k fluctuations can produce plasma transport through multiple channels. Particularly, it can produce significant ion thermal transport of experimental level in the outer core region (lower-left panel of Fig. 8). It is interesting to note that in similar DIII-D L-mode discharges, a so-called transport "shortfall" was found when comparing the results of gyrokinetic simulations and the measured ion heat flux in the outer core region. [27, 28] As shown in the lower-left panel of Fig. 8, the sum of KH/ITG fluctuation driven transport and neoclassical transport which is calculated from a global GTC-NEO simulation, including finite orbit width effect,[29] can reproduce experimental χ_i profile fairly well (within a factor of two) without considerable transport "shortfall" in the outer core region. On the other hand, KH/ITG driven transport contributes weakly to the experimentally observed electron thermal transport, which is usually highly anomalous and dominates over the ion channel transport in NSTX. The cause for the highly anomalous electron thermal transport remains a critical issue under investigation.

IV. DISSIPATIVE TRAPPED ELECTRON MODE AND TURBULENCE

Magnetically trapped particles play many important roles for equilibrium, stability and transport of plasmas in toroidal devices. In particular, the presence of trapped electrons give rise to specific electron drift wave instabilities, the so-called trapped electron modes (TEM), which are one of the major causes for anomalous plasma transport. There are two types of TEM instabilities associated with different trapped electron dynamics.[30] In the range of relatively low collision frequency (in comparison to the characteristic frequencies of plasma

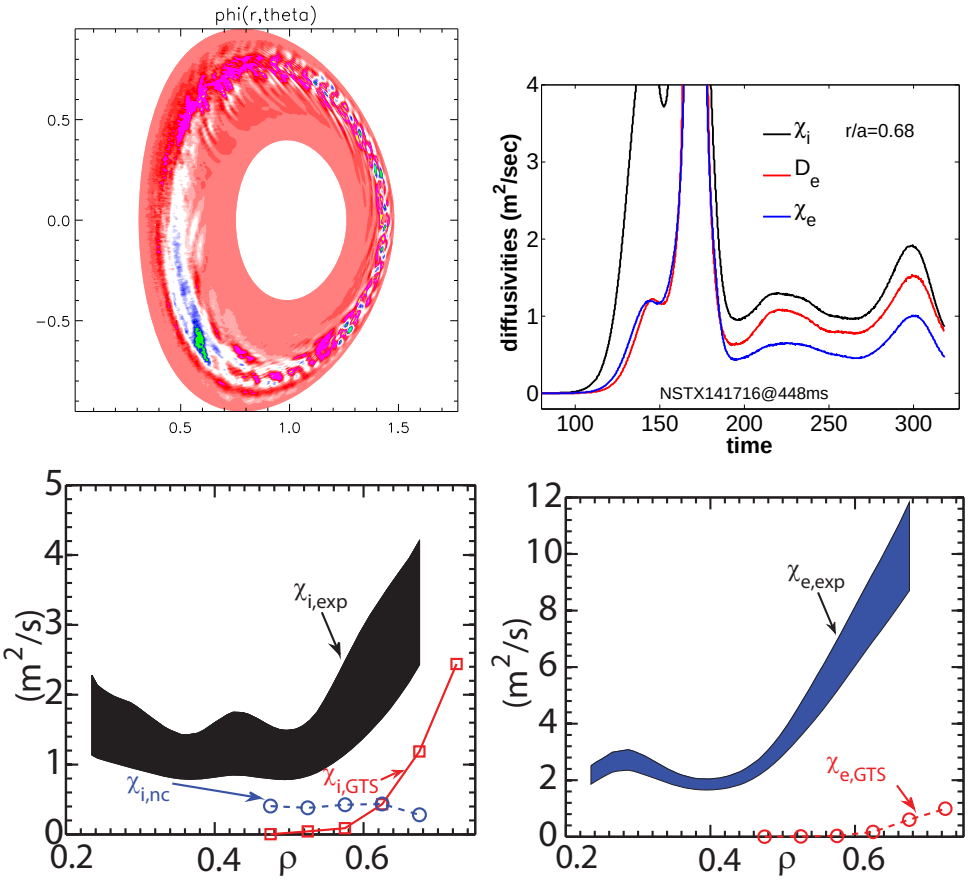

FIG. 8: Contour plot of electric potential during well-developed KH/ITG turbulence (upper-left); time history of ion thermal, particle and electron thermal diffusivity of turbulence-driven transport at $r/a = 0.68$ (upper-right); radial profile of turbulence-generated and neoclassical ion thermal diffusivity (lower-left), and turbulence-generated electron thermal diffusivity (lower-right) in comparison with experimental values from TRANSP analysis.

motion) that current tokamak experiments cover, a drift wave instability can be excited through the trapped electron magnetic processional drift resonance with the mode. This is the so-called "collisionless trapped electron mode" (CTEM), which, along with the well-known ITG mode, is believed to be a major source for low-k ($k_\theta \rho_i \sim 1$ or lower) fluctuations and associated turbulent transport widely observed in tokamak devices. Another electron drift wave instability arises from a dissipation mechanism due to electron collisions, which destabilizes the mode through the scattering of trapped electrons into transit electrons. This is the so-called "dissipative trapped electron modes" (DTEM). Both CTEM and DTEM are

driven by the free energy provided by electron density and temperature gradients. Collisions may also have a significant impact on CTEM, linearly through electron drift precession, and nonlinearly through zonal flow damping.

A. Identification of DTEM and its outstanding features in NSTX

The strength of CTEM and DTEM depends on the trapped electron fraction $\sim (a/R)^{1/2}$ [more precisely, the growth rate is roughly proportional to $(a/R)^{1/2}$]. CTEM is found to be important in almost all present tokamaks. On the other hand, as pointed out previously by linear calculation,[31] the excitation of DTEM requires very steep electron density or temperature gradients at the collisionality regime relevant to present tokamaks, which can hardly be achieved for typical parameters of conventional tokamak regime. Indeed, there is little experimental evidence, at least in the core region of tokamak plasmas, showing DTEM to play a role in driving transport. In low aspect ratio STs, the trapped particle fraction can be much higher than in conventional tokamaks. This may make TEMs more important as turbulence sources in STs. Our investigation shows that DTEM is more likely to be present in ST regimes and make significant contributions to plasma transport and confinement features, while CTEM is subject to strong collisional stabilization in the typical parameter regime of present ST experiments. This is the opposite situation of conventional tokamaks.

Our investigation using gyrokinetic simulations is carried out for an NBI-heated NSTX H-mode discharge with strong toroidal rotation.[32] As shown in Fig. 9, there is strong electron gradients, in particular the density gradient presented in the central core region. In the same radial area there is also a very strong toroidal rotation shear, and a correspondingly strong $\mathbf{E} \times \mathbf{B}$ shear. The large gradient in density is due to the temporal proximity to an edge localized mode, but a DTEM is predicted to occur at this density gradient value as well as values that are lower by a factor of three. Unlike the L-mode discharge we studied in the previous section, the KH mode is not excited by the toroidal rotation shear in this case, mainly because of the presence of strong density gradient, which stabilizes the mode. On the other hand, the strong density gradient is found to drive TEM unstable in the region. Distinguishing DTEM from CTEM is made through mode reactions to electron collisions. Our global simulations cover $\rho = 0.3 \ - \ 0.8$ with focus on $\rho \lesssim 0.65$ (experimental data for the T_i profile is not accurate for this shot in the outer region beyond this point). Figure 10

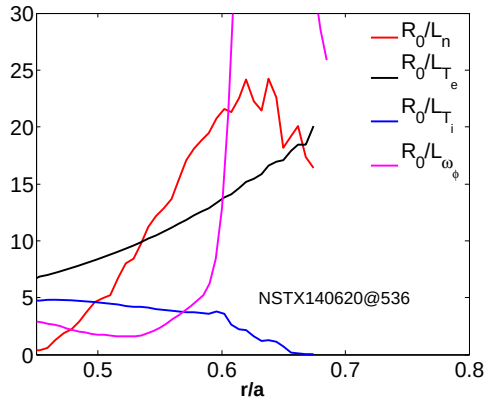

FIG. 9: Radial profile of plasma gradients R_0/L_n, R_0/L_{T_e}, R_0/L_{T_i} and R_0/L_{ω_ϕ} for the NSTX H-mode discharge 140620 at 536 msec.

presents the results of mode structure in the linear phase for four nonlinear simulations of the same discharge. These simulations are almost identical except for one control parameter, which is used to turn collisions on or off. The results clearly show how collisions turn ∇n-driven instability from CTEM to DTEM. When both electron and ion collisions are set to be zero, the instability excited is CTEM (upper-left panel of Fig. 10). The poloidal wavenumber for the most unstable CTEM mode is $k_\theta \rho_s \sim 0.5$, as indicated in the upper-middle panel of Fig. 10. As we turn on both electron and ion collisions, the unstable modes switch to ones with much larger structures (lower-left panel of Fig. 10), which are clearly different from CTEM. The most unstable mode now peaks at $k_\theta \rho_s \sim 0.1$, as indicated in the lower-middle panel of Fig. 10. Moreover, what destabilize the longer wavelength modes are electron collisions rather than ion collisions. As shown in the upper panels of Fig. 10, the unstable modes remain CTEMs when there is no electron collisions and that, even if the ion collisions are present (upper-right panel). However, the presence of electron collisions is required for the longer wavelength modes to be unstable (lower panels of Fig. 10) and the ion collisions have little effect on that process. All these features identify DTEM as the long wavelength modes observed in the simulations of NSTX H-modes with real collision frequencies, which are driven by electron gradients and destabilized by electron collisions.

More interesting linear features of DTEM in comparison with CTEM are presented in Fig. 11 which shows the real frequency and growth rate as a function of $k_\theta \rho_s$. First, DTEM is seen to be clearly separated from CTEM in k-space, as also shown by the spatial scale separation

between them in Fig. 10. The scale separation from other low-k modes may be utilized for identifying DTEM in ST experiments. Both DTEM and CTEM have a real frequency close to the ion bounce frequency, $\omega \sim \omega_{b,i}$, falling into the so-called transition regime which is usually not covered by analytical theory. Indeed, the linear property of DTEM in NSTX differs significantly from the dispersion relation of DTEM originally derived by Kadomtsev and Pogutse in very restricted parametric regimes:[33]

$$\omega \simeq \omega_{*e} + i\sqrt{\epsilon}\frac{6}{\sqrt{\pi}}\frac{\eta_e \omega_{*e}^2}{(\nu_{ei}/\epsilon)}. \tag{12}$$

where ω_{*e} is the electron diamagnetic drift frequency and $\eta_e = |\nabla \ln T_e / \nabla \ln n_e|$. For example, Eq. 12 indicates the real frequency $\sim \omega_{*e}$ which increases with k_θ, and the growth rate $\sim 1/\nu_{ei}$, indicating that electron collisions stabilize the mode. One most remarkable feature illustrated in Fig. 11 concerns the $\mathbf{E}\times\mathbf{B}$ shear effect on the instabilities. As indicated by the finite growth rates calculated with the equilibrium E_r included in Fig. 11, both CTEM and DTEM can survive the strong experimental $\mathbf{E}\times\mathbf{B}$ shear mainly due to strong NBI-induced toroidal rotation. However, the $\mathbf{E}\times\mathbf{B}$ shear destabilization effect on DTEM is surprisingly weak (almost negligible). On the other hand, the $\mathbf{E}\times\mathbf{B}$ shear can reduce the CTEM growth rate by a factor of ten. Unlike the normal broad-band fluctuations such as ITG and CTEM, the DTEM observed in NSTX shows a large scale, quasi-coherent eddy structure with a few dominant modes, which may make it less sensitive to $\mathbf{E}\times\mathbf{B}$ shear. Moreover, unlike the typical ballooning structure, which is located at the low-field side mid-plane region, DTEM appears to also balloon in the region of both top and bottom tips (see Fig. 10), probably due to additional magnetic wells at the location in NSTX. This may make the $\mathbf{E}\times\mathbf{B}$ shearing effect, which is poloidal-angle dependent, weaker. Nevertheless, the strong survivability of DTEM may make it, in ST regime, a major turbulence source dominant over CTEM, the latter is also subject to strong collisional stabilization in NSTX, in additional to the normal $\mathbf{E}\times\mathbf{B}$ shear suppression effect.

On the other hand, DTEM is found to be hardly destabilized in the conventional tokamak regime, as was pointed out previously.[31] Figure 12 presents a comparable example in conventional tokamak. The comparable case is generated using a realistic DIII-D geometry, combined with the same NSTX plasma gradient profiles as in Fig. 9. In order to match the typical temperature level of DIII-D plasmas, the NSTX ion and electron temperatures are multiplied by a factor of 3 for the purpose of this case. Four simulations are carried out,

varying the electron collision frequency from zero to 40 times the real frequency (corresponding to the electron temperature and density). As shown by the unchanged mode structure (upper left and right panel of Fig. 12), CTEM is persistently present and DTEM excitations are not observed over a wide range of electron collisionalities. Increasing the collisionality does not cause a mode switch from CTEM to DTEM, but decreases the CTEM growth rate (lower-left panel of Fig. 12), and consequently, the CTEM turbulence-driven transport level (lower-right panel of Fig. 12).

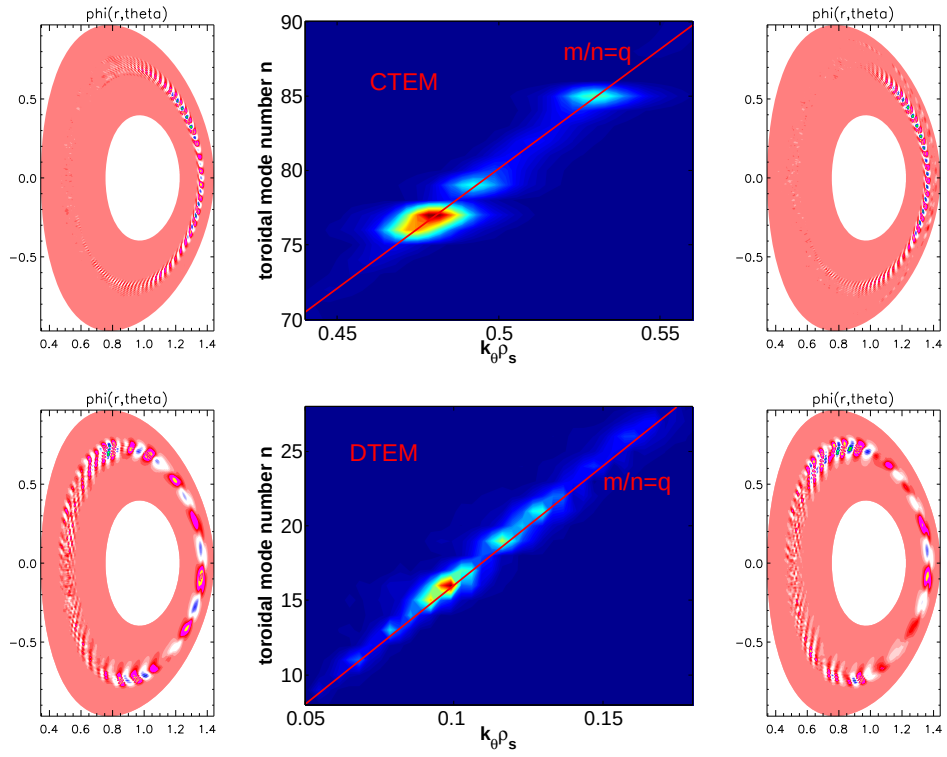

FIG. 10: Contour plot of electric potential showing the linear mode structures of four simulations using different collision frequencies for the NSTX case in Fig. 8: $\nu_i = \nu_e = 0$ (upper-left), $\nu_i = 1$ and $\nu_e = 0$ (upper-right), $\nu_i = 1$ and $\nu_e = 1$ (lower-left), and $\nu_i = 0$ and $\nu_e = 1$ (lower-right). Here, ν_i and ν_e are normalized by the realistic ion and electron collision frequency, respectively. Also plotted are the linear mode spectra $\delta\Phi^2_{mn}$ for the $\nu_e = 0$ case (upper-middle) and for the $\nu_e = 1$ case (lower-middle).

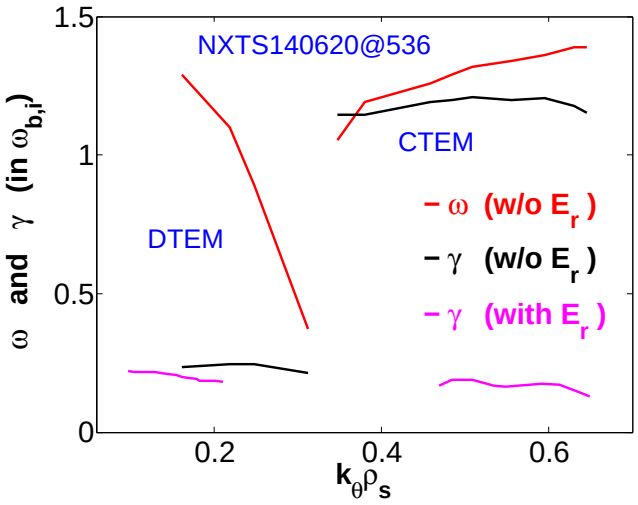

FIG. 11: Linear growth rate γ and real frequency ω (normalized by ion bounce frequency $\omega_{b,i}$) vs poloidal wavenumber k_θ for DTEM and CTEM from simulations with $\nu_e = 1$ and $\nu_e = 0$, respectively.

B. Contribution of DTEM turbulence to NSTX transport

Nonlinearly, the saturation of DTEM is accompanied with a significant spectrum downshift and zonal flow generation – a quite robust phenomenon widely observed in various drift wave turbulence.[34–36] Compared to the CTEM case (namely, using $\nu_e = 0$), the zonal flow generation in DTEM turbulence seems more efficient. This is indicated by the ratio of zonal flow energy and turbulence energy growth rate at the turbulence developing phase, which is 1.98 for DTEM vs 1.52 for CTEM, as measured around the radial location of peaked instability drive. Meanwhile, the zonal flow in CTEM appears to have finer radial structures (smaller k_r) than that of DETM. Furthermore, like the equilibrium $\mathbf{E} \times \mathbf{B}$ flow, DTEM self-generated zonal flows are observed to have weak effects on turbulence decorrelation. Consistently, the saturated DTEM turbulence shows large scale, quasi-coherent eddy structure as seen in a potential contour plot (left on Fig. 13), with a narrow spectrum consisting of a few dominant modes at a low-n range corresponding to $k_\theta \rho_s \sim 0.03 - 0.08$ (right on Fig. 13). This characteristic distinguishes DTEM from other low-k turbulence, and can be utilized for its identification in experiments. The quasi-coherent DTEM fluctuations are shown to drive significant plasma transport in multiple channels. The simulated DTEM-driven fluxes are compared with the experimental values deduced from power, par-

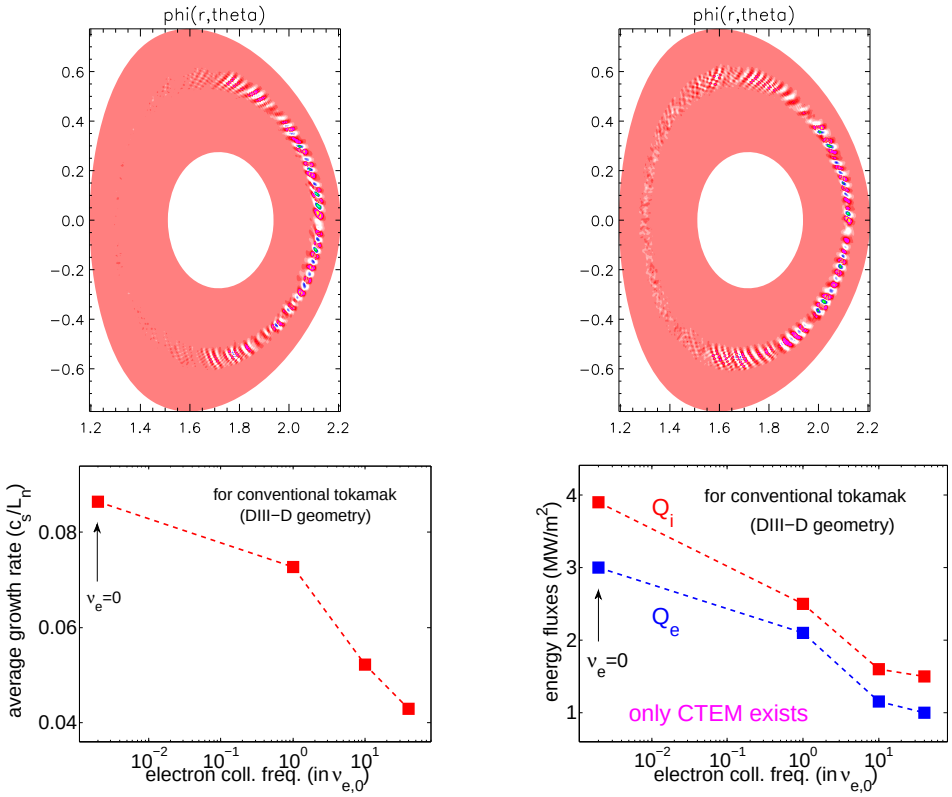

FIG. 12: Simulation results of a comparable case for conventional tokamak using a DIII-D geometry along with the same NSTX density and temperature gradients as in Fig. 9: Contour plot of electric potential at linear phase for $\nu_e = 0$ (upper-left) and $\nu_e = 40$ (upper-right) showing persistent CTEM instability with no DTEM presented. Also plotted are the average mode growth rate (lower-left) and saturated ion and electron energy flux (lower-right) as a function of electron collision frequency.

ticle and momentum balance based on measurement data in Fig. 14. It is observed that the DTEM-generated ion energy flux is quite close to the experimental value, and DTEM-induced particle and momentum transport are also close to experimental level in the central core region where DTEM is unstable. However, the density gradient driven DTEM in this case appears not to produce enough transport to account for the highly anomalous electron energy flux in experiments. The simulated electron energy flux is about four times lower than the experimental level estimated from TRANSP analyses. It should be noticed that DTEM can also be driven by the free energy provided by electron temperature gradient in the ST parametric regime. In such cases, it is possible that DTEM turbulence may generate large energy transport for electrons. To demonstrate this, an example using the previous

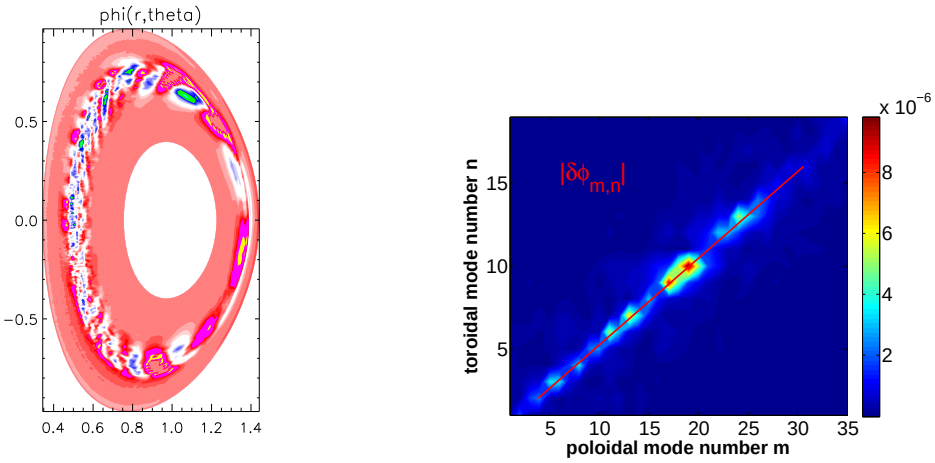

FIG. 13: The snapshot of fluctuation potential at saturated DTEM turbulence (left) and spectrum $\delta\Phi_{mn}$ (right) from a nonlinear simulation of NSTX discharge in Fig. 9.

H-mode equilibrium along with the plasma profiles of a reverse magnetic shear discharge where a strong electron temperature gradient is present in the inner core region, forming an internal transport barrier,[37, 38] is studied. The strong electron temperature gradient in the inner core region around $r/a = 0.3$ (upper-right panel of Fig.15) is shown to destabilize either CTEM or DTEM, depending on the electron collision frequency. For realistic collision frequencies, DTEM is destabilized (lower-left and middle panels of Fig. 15), and CTEM, which is present at artificially reduced electron frequency (upper-left panels of Fig.15), is stabilized. Compared to linear CTEM modes, which show a broad-band spectrum peaking at around $k_\theta\rho_s \sim 1$ (upper-middle panel of Fig.15), DTEM consists of several dominant lower-n modes at $k_\theta\rho_s \sim 0.55$ and 0.65 (lower-middle panel of Fig.15), showing quasi-coherent features. As shown in the lower-right panel of Fig. 15, ∇T_e-driven DTEM fluctuations are found to produce large electron thermal transport, with χ_e value a few times higher than that produced by the ∇n-driven DTEM fluctuations in the previous case. Therefore, it is possible that DTEM may drive a large electron energy transport.

It is also noticed that DTEM turbulence may drive an intrinsic toroidal rotation as significant residual stress generation due to DTEM fluctuations is observed in these simulations. However, the strong toroidal rotation in such NSTX discharges is largely driven by the external NBI torque, and the contribution of intrinsic rotation is small. Furthermore, given that the $\mathbf{E}\times\mathbf{B}$ shear effects on DTEM are weak, we expect that the effect of intrinsic rotation via

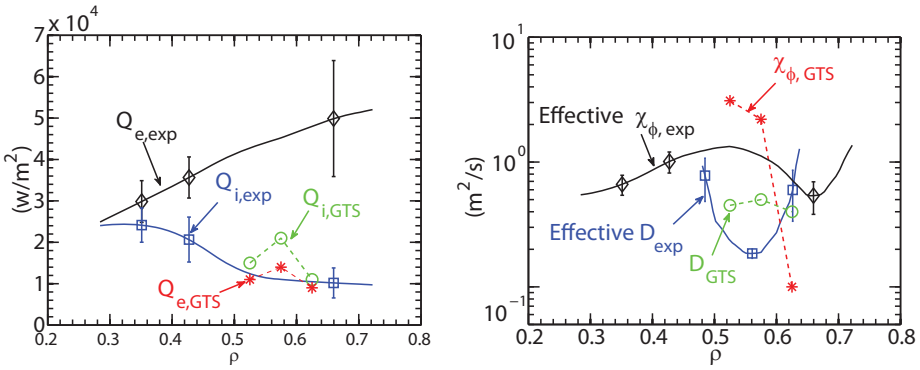

FIG. 14: Simulated DTEM driven ion and electron energy flux (left), and particle and effective toroidal momentum diffusivity (right) in comparisons with experimental values deduced from TRANSP analysis.

its contribution to the equilibrium $\mathbf{E}\times\mathbf{B}$ shear on DTEM turbulence is weak. On the other hand, DTEM driven intrinsic rotation may impact other low-k turbulence such as ITG and CTEM in non-NBI-heated ST plasmas. We leave this interesting issue for future studies.

V. COLLISIONALITY DEPENDENCE OF TEM-DRIVEN TRANSPORT AND CONFINEMENT SCALING IN SPHERICAL TOKAMAKS

We have shown that DTEM may provide a robust turbulence source for driving transport in ST regime. The roles of collisions played in DTEM are subtle and non-trivial.[39] It is highly interesting to examine how DTEM-driven transport depends on collisions, in particular whether DTEM can contribute to the confinement scaling of ST devices. Note that the effect of DTEM on energy confinement in tokamaks was discussed.[40] In NSTX, the energy transport is usually dominated by the electron channel, particularly in H-modes. It has observed that the energy confinement time τ_E in NSTX is proportional to the inverse of the electron collisionality $\nu_{*,e}$, more specifically $B_T\tau_E \sim \nu_{*,e}^{-0.79}$.[41] This scaling was observed in NSTX H-mode discharges and will be further tested in the lower collisionality regime of NSTX-U experiments. It predicts a higher performance for future advanced STs in burning plasma regime compared to conventional large aspect ratio tokamaks, such as ITER. Understanding the underlying mechanism remains a critical issue for experimental and theoretical research, which contributes to the important knowledge base needed for developing future

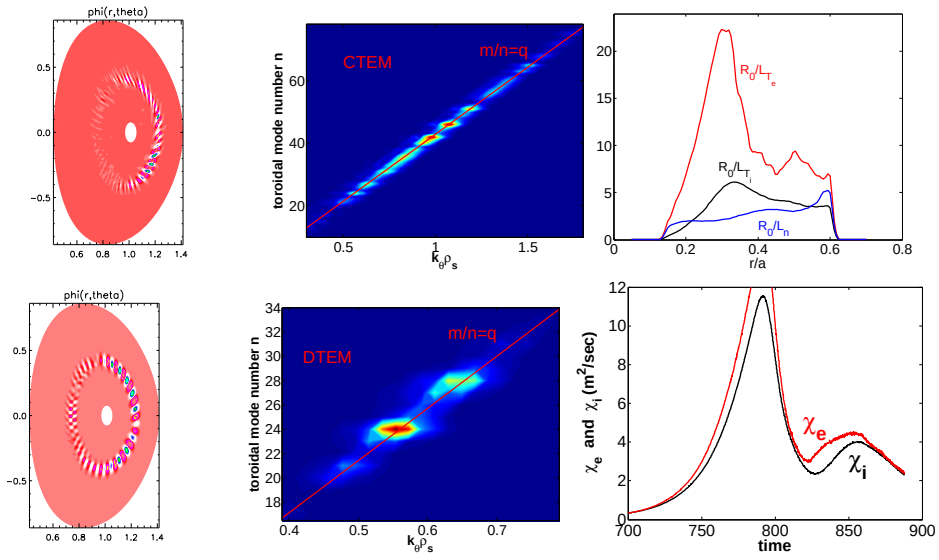

FIG. 15: Results of a ∇T_e-driven TEM case with NSTX parameters from two nonlinear simulations using different electron collision frequency: radial profile of various plasma gradients R_0/L_{T_i}, R_0/L_{T_e}, R_0/L_n (upper-right); contour plot of electric potential at a linear phase (upper-left) and corresponding spectrum $\delta\Phi^2_{mn}$ (upper-middle) for $\nu_e = 0$; contour plot of electric potential at a linear phase (lower-left) and corresponding spectrum $\delta\Phi^2_{mn}$ (lower-middle) for realistic electron collision frequency $\nu_e = 1$; time history of simulated DTEM-driven electron and ion thermal diffusivity with $\nu_e = 1$ (lower-right).

advanced ST experiments. It has been proposed that the micro-tearing instability, which is driven by the electron temperature gradient and destabilized by electron collisions, may introduce the $1/\nu_{*,e}$-scaling.[42] However, it is also shown that the strong $\mathbf{E} \times \mathbf{B}$ shear in NSTX can strongly suppress the micro-tearing instability.

On the other hand, DTEM, which is also destabilized by electron collisions in NSTX regime, can well survive the experimental, high level of $\mathbf{E} \times \mathbf{B}$ shear, providing a possible candidate contributing to the observed confinement scaling. A series of nonlinear simulations using the H-mode case of Fig. 9 are carried out for a collisionality scan, varying the electron collision frequency from zero to four times the realistic electron frequency. As shown in Fig. 16, a change in the electron collision frequency causes a turbulence transition from CTEM to DTEM. CTEM turbulence is only present in very collisionless regimes that are not accessible by NSTX. This suggests that CTEM probably play little role in NSTX and

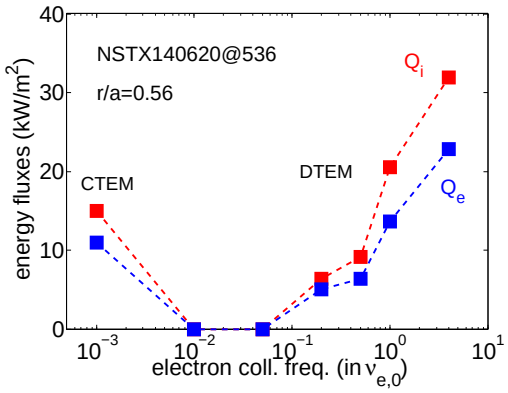

FIG. 16: Simulated TEM-driven ion and electron energy fluxes as a function of normalized electron collision frequency. Note that the CTEM data points actually correspond to the use of zero electron collision frequency. These simulations are performed for the NSTX case in Fig. 9.

its upgrade NSTX-U. In the collisionality range that NSTX plasmas operate in, DTEM turbulence is dominant. DTEM-driven transport in all channels, including electron and ion energy fluxes, are shown to increase close to linearly as the electron collisionality increases. This indeed gives the same trend as the confinement time scaling obtained from the NSTX H-mode database. The physics behind this result is quite straightforward. Namely, collision-induced destabilization of DTEM becomes stronger as electron collisions increase in NSTX parametric regime. In contrast, CTEM-induced transport in the conventional tokamak regime gives an opposite trend, as is shown in Fig. 12. This result suggests that in electron-heated burning plasmas in tokamaks, such as the ITER regime where CTEM may become a dominant turbulence sources, the plasma confinement may degrade as the heating power increases. One highly interesting result found from this collisionality scan study is that there exists a unique parametric range in collision-induced "CTEM to DTEM" transition in ST plasmas, where electron collisions are high enough to fully stabilize CTEM, but not too high to excite DTEM. If ST experiments are operated in this turbulence-free regime, in principle it may allow access to a minimum transport state and achieve high plasma confinement. Corresponding to this minimum transport state in collision-induced CTEM to DTEM transition, the electron collision frequency is about one to two orders of magnitude lower than that of NSTX plasmas, which may correspond to the collisionality regime of future advance STs.

VI. DISCUSSION ON THE EFFECT OF SHORT SCALE FLUCTUATIONS ON THE CONFINEMENT SCALING

In this section, we discuss the role of electron gyroradius scale turbulence in NSTX, in particular, its possible contribution to the confinement scaling based on insights obtained from nonlinear simulations of short scale turbulence.

Short scale fluctuations were identified in NSTX experiments by high-k micro-wave coherent scattering measurements,[43] which are linked to electron temperature gradient (ETG) mode driven turbulence. Global, nonlinear simulations of ETG turbulence for experimental discharges were carried out for direct validation against the high-k fluctuation measurements in NSTX, and quantitatively testing the role of ETG for driving anomalous electron energy transport in experiments.[44] Global kinetic simulation of electron scale turbulence in a real fusion device is highly challenging. To reduce the excessive computational cost, our global ETG simulations used adiabatic ions, neglecting couplings between ETG and low-k turbulence. The simulated ETG density fluctuations show a $k_\perp$ spectrum in general agreement with experimental measurements in the range of $k_\perp \rho_s \sim 5 - 15$, which is the range that the high-k scattering diagnosis covers. The simulations also indicate a significant ETG-induced contribution to anomalous electron heat transport in NSTX, as shown in Fig. 17. One remarkable new feature observed from these nonlinear ETG simulations is that there exists direct, strong energy coupling between high-k ETG modes and electron geodesic acoustic modes (e-GAMs with high frequency and poloidal mode number $m = 1$ in density perturbation). This can be clearly seen in Fig. 18, which illustrates the nonlinear spectral evolution in 2-dimensional perpendicular wavenumber space ($k_r,\ k_\theta$) of the density fluctuations in a small area located on the mid-plane as ETG develops. During the linear phase, the mostly unstable ETG modes are excited at around $k_\theta \rho_s \sim 13$, with strong anisotropy in the spectrum, namely, $k_r \ll k_\theta$ (left penal of Fig. 18), corresponding to radially elongated streamers in real space. When the instability reaches saturation, the ETG energy is remotely transferred (in k-space) to the $m = 1$ e-GAM mode via nonlinear mode coupling. At the well-developed turbulence state, the fluctuation spectrum downshifts and peaks at $k_\theta \rho_s \sim 6$, along with the presence of strong e-GAM. During this process, a low frequency zonal flow with fine radial scale is also generated and continuously grows, which co-exists with radially elongated streamers in the nonlinear phase of ETG turbulence. This direct

energy channeling from ETG to e-GAM and low frequency zonal flows observed in the simulations may represent an effective mechanism for nonlinear ETG saturation, suggesting that the collisional damping of zonal flows and e-GAMs may have an impact on the formation of the steady state fluctuation spectrum and saturation level. Direct dependence of ETG on electron collisionality is weak. However, the effect of electron collisions on ETG-driven transport could be introduced via collisional zonal flow and e-GAM damping, in analogy to the well-known paradigm of zonal flow regulating fluctuations in ITG turbulence. An example that ion collisions influence fluctuation-driven transport in ITG turbulence is presented in Fig. 19, which is obtained from global simulations of a DIII-D discharge where a significant ion temperature gradient in the inner core region drives the instability. The simulations include kinetic electrons and consistent neoclassical physics. The increase of ITG-driven ion thermal transport with the increase of ion collisions is attributed to the decrease of zonal flow amplitude due to enhanced collisional damping. Also noticed in Fig. 19 is that the collision effect on ITG-driven ion transport becomes weaker or negligible at lower collisionality regime. This is because of the separation between the time scale for zonal flow collisional damping and the time scale for turbulence to develop. As we move to a lower collisionality regime, the former becomes much longer than the latter. In experiments, a similar strong dependence of ITG-driven ion heat flux on ion collisions was also observed in ion-transport dominated H-mode discharges.[45, 46] Given that strong, direct coupling between ETG modes and e-GAMs and zonal flows may exists, it is a reasonable to expect that a similar mechanism for electron collisions to influence fluctuation-driven electron transport may occur in ETG turbulence, which may possibly lead to the scaling of confinement time proportional to $1/\nu_{*,e}$. This mechanism is subject to further investigations to verify, using nonlinear ETG simulations, scanning with electron collision frequency.

VII. SUMMARY AND DISCUSSION

Nonlinear global gyrokinetic simulations of NSTX experiments have identified two distinct turbulence sources responsible for plasma transport in the unique spherical tokamak regime. Compared to conventional tokamaks of larger sizes, momentum injected through neutral beam heating can rotate the plasma toroidally much faster in NSTX, with a Mach number $M \sim 1$, along with steep gradient in the core region. Such a strong toroidal rotation is shown

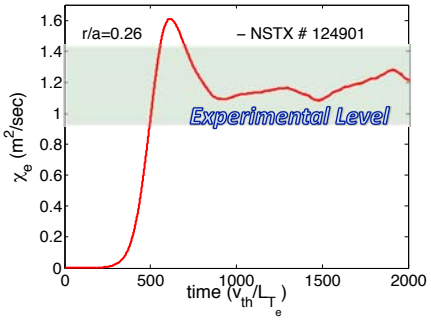

FIG. 17: Time history of χ_e from a global ETG simulation of an NSTX discharge and comparison with experimental estimate.

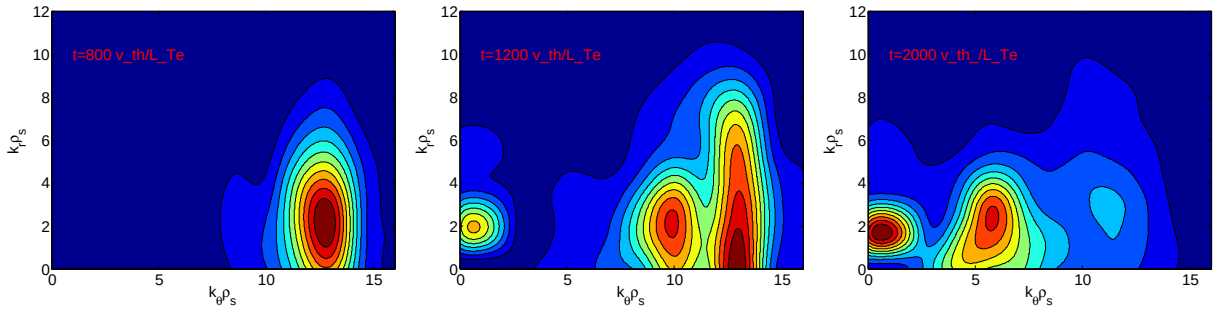

FIG. 18: Time evolution of 2D spectra of density fluctuations from an ETG simulation of NSTX, showing direct energy coupling from ETG to e-GAM.

to destabilize drift-wave Kelvin-Helmholtz modes in NSTX L-modes. For the first time, the Kelvin-Helmholtz mode is found to be relevant to realistic fusion experiments. Clear identification of the KH mode in NSTX is made through its characteristic mode structure, which has an intrinsic asymmetry with respect to the mode rational surface, a unique feature that distinguishes itself from other drift wave modes, such as ITG, which is also unstable in the NSTX case we studied and in the same range of wavelengths as that of KH. Nonlinearly, KH instability is saturated through energy transfer to longer wavelength, linearly stable modes via toroidal mode coupling, along with strong zonal flow generation, a quite robust paradigm observed in most drift wave turbulence systems. On the other hand, the strong rotation gradient creates a $\mathbf{E} \times \mathbf{B}$ shear, which is shown to reduce KH/ITG-produced low-k fluctuations and associated transport both linearly by changing the unstable mode family

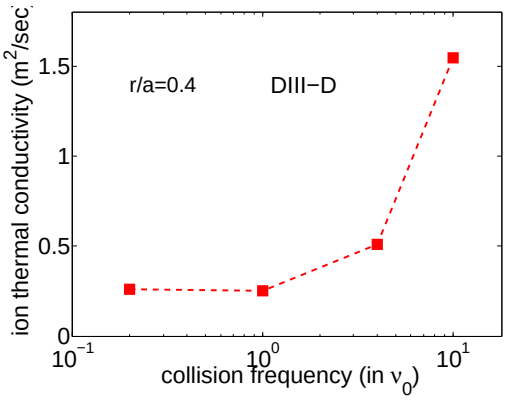

FIG. 19: Calculated ITG turbulence driven ion thermal conductivity as a function of normalized ion collision frequency from global simulations of a DIII-D discharge.

members and structure, and nonlinearly by modifying fluctuation amplitude and spectrum. However, even at the reduced level, the remaining low-k fluctuations can drive transport in multiple channels for NSTX plasmas, in particular, a significant ion thermal transport (larger than neoclassical one) relevant to experimental level in the outer core region (no ion transport "shortfall" observed). We also note that KH/ITG turbulence contributes weakly to the observed, highly anomalous electron thermal transport in NSTX.

The other new, important turbulence source identified in NSTX is the dissipative trapped electron mode, which is shown to be hardly destabilized and believed to play little role in typical parameter regimes of conventional tokamak. Partially due to the high trapped electron fraction, long wavelength DTEMs are destabilized in NSTX collisionality regime by large electron density and temperature gradients achieved in H-mode plasmas. On the other hand, collisionless trapped electron mode, which is driven by the same free energy provided by electron pressure gradients, is fully stabilized by collisions in NSTX regime. Compared to CTEM, DTEM's poloidal wavelengths are about 2 -5 times longer. The clear spatial scale separation can be helpful for its identification in experiments. One most remarkable feature of DTEM is that the normal $\mathbf{E} \times \mathbf{B}$ shear destabilization effect on the mode is surprisingly weak, if not negligible. This allows DTEM to survive the strong $\mathbf{E} \times \mathbf{B}$ shear associated with large toroidal rotation in NSTX, and become a major turbulence source dominant over other low-k modes such as ITG and CTEM. In contrast to the broad-band fluctuations of typical ITG and CTEM turbulence, DTEM fluctuations exhibit the features of quasi-

coherent modes, consisting of several dominant low-n modes. This characteristic can also be used as a fingerprint for its experimental identification. DTEM fluctuations are shown to contribute significant transport to ion energy, particle and toroidal momentum, in reasonable agreement with experimental level in H-mode. We also show that, for certain plasma parameters, DTEM can possibly drive a large electron energy flux of experimental level in NSTX. More interestingly, in the NSTX collisionality regime, DTEM-driven transport is shown to decrease with a decrease in electron frequency. Given that DTEM could be robustly present in NSTX H-modes, this result suggests that DTEM may provide one possible source for the experimentally observed scaling of confinement time inversely proportional to the electron collisionality. In contrast, the collisionality dependence of CTEM-driven transport in conventional tokamak regimes shows an opposite trend, which may suggest a possible mechanism for confinement degradation in electron heated burning plasmas as the heating power increases (electron temperature goes up). In addition, our discussion is extended to the collisional effect on electron transport produced by short scale fluctuations due to ETG turbulence. The existence of direct energy channeling from ETG to e-GAM and zonal flow as observed in our nonlinear ETG simulations of NSTX give rise to a way by which electron collisions can affect ETG-driven transport through collisional zonal flow damping. Interestingly, we show that there exists a turbulence-free regime in collision-induced CTEM to DTEM transition for ST plasmas, in which the collisional drive mechanism is not strong enough to excite DTEM in the one hand, and the collisionless drive mechanism (magnetic drift resonance), on the other hand, is also too weak to excite CTEM. This predicts a natural access to a minimum transport state in the low collisionality regime that future advanced STs may cover.

It is interesting to note that the long wavelength trapped ion mode (TIM) [47] with the mode frequency lower than the ion bounce frequency may also be present and play a role in ST regimes due to a high fraction of trapped ions. In particular, the dissipative TIM, which is destabilized by electron collisions and damped by ion collisions when the effective collision frequency of trapped particles exceeds the magnetic drift frequency, is more relevant and could possibly impact the ST confinement scaling. Meanwhile, the collisionless ITM at very high temperature regime, which does not directly involve collisions, could be less relevant. Identifying ITMs and their roles in STs would be an interesting subject for future studies. Finally, we point out that our current nonlinear gyrokinetic studies focus on the

electrostatic turbulence regime. It would be highly interesting to investigate how KH and DTEM turbulence and transport are modified by electromagnetic effects due to high-β values in ST plasmas. This is a largely unexplored topic which should be addressed in the future.

ACKNOWLEDGMENTS

Useful discussions with Drs. T. S. Hahm, G. Rewoldt, X. Tang, W. W. Lee, G. Hammett, and W. Guttenfelder are acknowledged. Simulations were performed on Edison at the National Energy Research Scientific Computing Center (NERSC). ETG simulations were carried out at OLCF. This work was supported by U.S. DOE Contract No. DE-AC02-09CH11466.

---

[1] S. M. Kaye, W. Solomon, R. E. Bell, B. P. LeBlanc, F. Levinton, J. Menard, G. Rewoldt, S. Sabbagh, W. Wang, and H. Yuh, Nucl. Fusion **49**, 045010 (2009).

[2] E. A. Belli, G. W. Hammett, and W. Dorland, Phys. Plasmas **15**, 092303 (2008).

[3] P. Angelino, X. Garbet, L. Villard, A. Bottino, S. Jolliet, Ph. Ghendrih, V. Grandgirard, B. F. McMillan, Y. Sarazin, G. Dif-Pradalier, and T. M. Tran, Phys. Plasmas **15**, 062306 (2008).

[4] W. X. Wang, Z. Lin, W. M. Tang, W. W. Lee, S. Ethier, J. L. V. Lewandowski, G. Rewoldt, T. S. Hahm, and J. Manickam, Phys. Plasmas **13**, 092505 (2006).

[5] W. X. Wang, P. H. Diamond, T. S. Hahm, S. Ethier, G. Rewoldt, and W. M. Tang, Phys. Plasmas **17**, 072511 (2010).

[6] A. J. Brizard and T. S. Hahm, Rev. Mod. Phys. **79**, 421 (2007).

[7] Y. Chen and R. B. White, Phys. Plasmas **4**, 3591 (1997).

[8] W. X. Wang, W. M. Tang, F. L. Hinton, L. E. Zakharov, R. B. White, and J. Manickam, Computer Phys. Communications **164**, 178 (2004).

[9] D. H. E. Dubin, J. A. Krommes, C. R. Oberman, and W. W. Lee, Phys. Fluids **26**, 556 (1983).

[10] W. W. Lee, Phys. Fluids **26**, 3524 (1983).

[11] P. W. Terry Rev. Mod. Phys. **72**, 109 (2000).

[12] R. E. Waltz G. D. Kerbel, and J. Milovich, Phys. Plasmas **1**, 2229 (1994).

[13] T. S. Hahm and K. H. Burrell, Phys. Plasmas **2**, 1648 (1995).

[14] N. D'Angelo, Phys. Fluids **8**, 1748 (1965).

[15] P. J. Catto, M. N. Rosenbluth, and C. S. Liu, Phys. Fluids **16**, 1719 (1973).

[16] J. F. Drake, A. H. Hassam, P. N. Guzdar, C. S. Liu, and D. MacCarthy, Nucl. Fusion **32**, 1657 (1992).

[17] M. Artun, and W. M. Tang, Phys. Fluids B **4**, 1102 (1992).

[18] J. Q. Dong, and W. Horton, Phys. Fluids B **5**, 1581 (1993).

[19] X. Garbet, C. Fenzi, H. Capes, P. Devnck, and G. Antar, Phys. Plasmas **6**, 3955 (1999).

[20] A. M. Dimits, B. I. Cohen, W. M. Nevins, and D. E. Shumaker, Nucl. Fusion **40**, 1725 (2001).

[21] M. Barnes, F. I. Parra, E. G. Highcock, A. A. Schekochihin, S. C. Cowley, and C. M. Roach, Phys. Rev. Lett. **106**, 175004 (2011).

[22] E. G. Highcock, A. A. Schekochihin, S. C. Cowley, M. Barnes, F. I. Parra, C. M. Roach, and W. Dorland, Phys. Rev. Lett. **109**, 265001 (2012).

[23] P. H. Diamond, C. J. McDevitt, O. D. Gurcan, T. S. Hahm, W. X. Wang, E. S. Yoon, I. Holod, Z. Lin, V. Naulin, and R. Singh, Nucl. Fusion **49**, 045002 (2009).

[24] J. Q. Dong, W. Horton, R. D. Bengtson, and G. X. Li, Phys. Plasmas **1**, 3250 (1994).

[25] J. Q. Dong, W. B. Xu, Y. Z. Zhang, and W. Horton, Phys. Plasmas **5**, 4328 (1998).

[26] Y. Ren, W. Guttenfelder, S. M. Kaye, E. Mazzucato, R. E. Bell, A. Diallo, C. W. Domier, B. P. LeBlanc, K. C. Lee, M. Podesta, D. R. Smith, and Y. Yuh, Nucl. Fusion **53**, 083007 (2013).

[27] C. Holland, A. E. White, G. R. McKee, M. W. Shafer, J. Candy, R. E. Waltz, L. Schmitz, and G. R. Tynan, Phys. Plasmas **16**, 052301 (2009).

[28] T. Rhodes, C. Holland, S. Smith, A. White, K. Burrell, J. Candy, J. DeBoo, E. Doyle, J. Hillesheim, J. Kinsey, G. McKee, D. Mikkelsen, W. Peebles, C. Petty, R. Prater, Y. Chen, L. Schmitz, G. Staebler, R. Waltz, G. Wang, Z. Yan, and L. Zeng, Nucl. Fusion **51**, 063022 (2011).

[29] W. X. Wang, G. Rewoldt, W. M. Tang, F. L. Hinton, J. Manickam, L. E. Zakharov, R. B. White, and S. Kaye Phys. Plasmas 13, 082501 (2006).

[30] B. B. Kadomtsev, and O. P. Pogutse, Nucl. Fusion **11**, 67 (1971).

[31] M. Romanelli, G. Regnoli, and C. Bourdelle, Phys. Plasmas **14**, 082305 (2007).

[32] Y. Ren, S. M. Kaye, E. Mazzucato, W. Guttenfelder, R. E. Bell, C. W. Domier, B. P. LeBlanc, K. C. Lee, N. C. Luhmann, Jr, D. R. Smith, and Y. Yuh, Phys. Rev. Lett. **106**, 165005 (2011).

[33] B. B. Kadomtsev, and O. P. Pogutse, Sov. Phys., Dokl **14**, 470 (1969).

[34] L. Chen, F. Zonca, and Z. Lin, Plasma Phys. Control. Fusion **47**, B71 (2005).

[35] Z. Lin, L. Chen, and F. Zonca, Phys. Plasmas **12**, 056125 (2005).

[36] W. X. Wang, T. S. Hahm, W. Lee, G. Rewoldt, J. Manickam, and W. M. Tang, Phys. Plasmas **14**, 072306 (2007).

[37] H. Y. Yuh, S. M. Kaye, F. M. Levinton, E. Mazzucato, D. R. Mikkelsen, D. R. Smith, R. E. Bell, J. C. Hosea, B. P. LeBlanc, J. L. Peterson, H. K. Park, and W. Lee, Phys. Rev. Lett. **106**, 055003 (2011).

[38] J. L. Peterson, R. Bell, J. Candy, W. Guttenfelder, G. W. Hammett, S. M. Kaye, B. LeBlanc, D. R. Mikkelsen, D. R. Smith, and H. Y. Yuh, Phys. Plasmas **19**, 056120 (2012).

[39] J. W. Connor, R. J. Hastie, and P. Helander, Plasma Phys. Control. Fusion **48**, 885 (2006).

[40] P. L. Similon and P. H. Diamond, Phys. Fluids **27**, 916 (1984).

[41] S. M. Kaye, S. Gerhardt, W. Guttenfelder, R. Maingi, R. E. Bell, A. Diallo, B. P. LeBlanc, and M. Podesta, Nucl. Fusion **53**, 063005 (2013).

[42] W. Guttenfelder, J. L. Peterson, J. Candy, S. M. Kaye, Y. Ren, R. E. Bell, G. W. Hammett, B. P. LeBlanc, D. R. Mikkelsen, W. M. Nevins, and H. Yuh, Nucl. Fusion **53**, 093022 (2013).

[43] E. Mazzucato, R. E. Bell, S. Ethier, J. C. Hosea, S. M. Kaye, B. P. LeBlanc, W. W. Lee, P. M. Ryan, D. R. Smith, W. X. Wang, J. R. Wilson, and H. Yuh, Nucl. Fusion **49**, 055001 (2009).

[44] S. Ethier, W. X. Wang, S. M. Kaye, E. Mazzucato, T. S. Hahm, G. Rewoldt, W. W Lee, and W. M. Tang, *Proc. of the 23rd IAEA Fusion Energy Conference, Daejon, Korea* (IAEA Vienna, 2010), IAEA-CN-165/TH-P4-08.

[45] M. Greenwald and G. M. Staebler, Plasma Phys. Controlled Fusion **40**, 789 (1998).

[46] C. C. Petty and T. C. Luce, Phys. Plasmas **6**, 909 (1999).

[47] B. B. Kadomtsev, and O. P. Pogutse, Sov. Phys. JETP **24**, 1172 (1967).